Semina Ciências Exatas e Tecnológicas

e-ISSN 1679-0375
ENGINEERING

ORIGINAL ARTICLE DOI 10.5433/1679-0375.2025.v46.53227

Numerical Simulations of High-lift Configurations on a NACA4412 Airfoil

Simulações Numéricas de Configurações de Alta-Sustentação em um Aerofólio NACA4412

Odenir de Almeida[1], Thiago Rezende de Castro[2]

Received: June 10, 2025 *Received in revised form: October 6, 2025* *Accepted: October 26, 2025* *Available online: December 15, 2025*

ABSTRACT

This work addresses the performance of different configurations of various high-lift devices applied to a NACA4412 airfoil, identifying their advantages and disadvantages. Numerical analyses with the CFD open-source code OpenFOAM® were carried out on five different configurations — namely, the plain flap, split flap, slotted flap, Fowler flap, and Junkers flap — under similar conditions, allowing for a consistent comparison of outcomes. All flaps were deflected by $10°$ and analyzed at a Reynolds number of 1.7×10^5 over a range of angles of attack between $-4°$ and $16°$. The Spalart–Allmaras turbulence model was used in all simulations, which were carried out in the steady-state regime. Quantitative results were analyzed for the coefficients of lift (C_l) and drag (C_d) per unit length and the pressure coefficient (C_p) on the surfaces of the analyzed airfoils, as well as the velocity and pressure flow fields. It was found that the simulations presented reliable and coherent results for lift and drag generation, but for angles of attack close to stall, convergence was more difficult. In addition, it was possible to identify the superiority in lift generation of the flap configurations most used in the aeronautical industry, such as the slotted flap and the Fowler flap.

keywords NACA4412, high-lift devices, aerodynamics performance, CFD, flap

RESUMO

Este trabalho aborda o desempenho de diferentes configurações de vários dispositivos de alta sustentação aplicados a um aerofólio NACA4412, identificando suas vantagens e desvantagens. Análises numéricas com o código aberto de CFD OpenFOAM® foram realizadas em cinco configurações diferentes — a saber, flap simples, flap dividido, flap com fenda, flap Fowler e flap Junkers — sob condições semelhantes, permitindo uma comparação consistente de resultados. Todos os flaps foram defletidos em $10°$ e analisados para um número de Reynolds de 1.7×10^5 em uma faixa de ângulos de ataque entre $-4°$ e $16°$. O modelo de turbulência Spalart–Allmaras foi usado em todas as simulações, que foram realizadas no regime de estado estacionário. Resultados quantitativos foram analisados para os coeficientes de sustentação (C_l) e arrasto (C_d) por unidade de comprimento e o coeficiente de pressão (C_p) nas superfícies dos aerofólios analisados, bem como os campos de escoamento de velocidade e pressão. Constatou-se que as simulações apresentaram resultados confiáveis e coerentes para geração de sustentação e arrasto, porém, para ângulos de ataque próximos ao estol, a convergência foi mais difícil. Além disso, foi possível identificar a superioridade na geração de sustentação das configurações de flap mais utilizadas na indústria aeronáutica, como o flap slotted e o flap Fowler.

palavras-chave NACA4412, dispositivos de alta-sustentação, desempenho aerodinâmico, DFC, flapes

---

[1] Prof. Dr., Department of Mechanical Engineering, UFU, Uberlândia, MG, Brazil. odenir.almeida@ufu.br

[2] Undergraduate student in Aeronautical Engineering, UFU, Uberlândia, MG, Brazil. thiagocastrowork@gmail.com

Introduction

The continuous pursuit of lighter and more efficient aircraft has placed high-lift devices at the core of aeronautical design. These systems directly influence payload capacity, takeoff and landing performance, and overall competitiveness in commercial aviation. As Meredith (1993) notes, a modest 1% increase in maximum lift coefficient can translate into an additional 22 passengers or roughly 2000 kg of payload. van Dam (2002) further emphasizes that, despite advances in laminar flow technology, high-lift systems will remain essential for the foreseeable future, ensuring aerodynamic efficiency across different flight regimes.

For decades, the aeronautical industry relied heavily on wind tunnel experiments to design and refine these devices. While experimental approaches provide valuable insight, they are increasingly limited by cost, time, and the difficulty of capturing unsteady and nonlinear phenomena such as boundary-layer transition, flow separation, recirculation, and reattachment.

These complexities have driven a shift toward Computational Fluid Dynamics (CFD) and optimization-based methodologies, enabled by advances in turbulence modeling, numerical schemes, and high-performance computing. CFD not only reduces cost and design cycle time but also provides greater flexibility for exploring configurations beyond the reach of traditional experimentation. Nevertheless, the application of CFD to high-lift aerodynamics remains challenging. Simulations at low Reynolds numbers require careful modeling of boundary-layer transition, while flows with adverse pressure gradients or narrow geometric gaps demand finely resolved meshes that balance numerical accuracy with computational feasibility. Furthermore, results remain sensitive to turbulence models, grid topology, and computational domain boundaries, introducing uncertainty into design evaluations.

A considerable body of literature has addressed these challenges for specific high-lift configurations. Studies have examined plain flaps on conventional airfoils such as the NACA 0012 and Eppler 423, highlighting differences between CFD solvers and panel methods (Bhandari, 2019; Fonseca et al., 2019; Kumar & Kumar, 2013). Others have incorporated experimental validation, such as Jawahar et al. (2018), who used Detached Eddy Simulation (DES) to study trailing-edge camber variations and associated unsteady effects.

Additional research has extended to wind turbine airfoils (Tan, 2020), Fowler flaps at low and high Reynolds numbers (Murayama & Yamamoto, 2004; Silva Oliveira, 2017), and three-element configurations combining slats, flaps, and main wings (Murayama et al., 2006; Sarjito et al., 2017). Collectively, these works demonstrate the promise of CFD in analyzing high-lift aerodynamics across scales and applications.

However, an important limitation persists: most studies are carried out under disparate conditions, employing different geometries, Reynolds numbers, turbulence models, and numerical frameworks. This lack of standardization makes it difficult to directly compare results, hindering the development of generalizable design guidelines or validated computational strategies.

Moreover, while individual studies often achieve agreement with experimental data for specific cases, a unified and robust methodology applicable across multiple high-lift configurations is still missing. To address this gap, the present work compiles and evaluates numerical analyses of various high-lift device configurations applied to a NACA 4412 airfoil under consistent conditions using OpenFOAM®. By doing so, it aims to establish a standardized framework for simulating flows around airfoils equipped with high-lift systems, bridging the fragmentation in the literature and providing a reliable methodology for future aerodynamic design.

Materials and methods

High-lift configurations and geometric model

High-lift devices are essential components in reducing take-off and landing distances for aircraft, found on most modern aviation aircraft, developed for use in different flight stages and making it possible to operate an aircraft at different airspeeds. In this work, a few commonly found configurations are discussed, which are presented in Figure 1.

Figure 1 - Different high-lift configurations: (a) plain flap, (b) split flap, (c) slotted flap , (d) fowler flap, and (e) junkers flap.

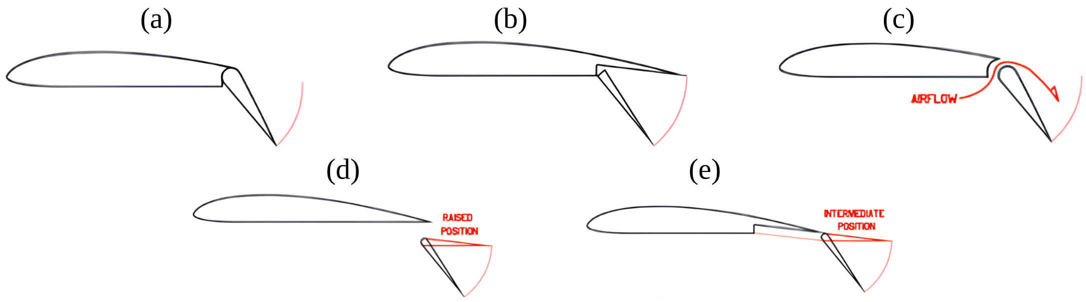

From "A retrospective of high-lift device technology. Proceedings of World Academy of Science" by A. Dal Monte, M.R. Castelli & E. Bnini, 2012, Engineering and Technology, (71).

The plain flap is the simplest geometry and is obtained by deflecting a portion of the trailing edge of the airfoil, while the split flap deflects only a portion of it around a point, while the rest remains fixed, Figures 1(a) and 1(b). The slotted flap is represented by a gap between the main element and the moving part. The deflection motion combines rotation and translation and increases the airfoil chord length by 5% to 10%, Figure 1(c). Considered a further development of the previous one, the Fowler flap moves backwards before fully deflecting, and finally, the Junkers flap is located entirely outside the wing. Both configurations increase the effective area by 25%, Figures 1(d) and 1(e).

Governing Equations

With simulations performed at a Reynolds number $Re = 1.7 \times 10^5$ and Mach number $Ma = 0.0029$, the flow is steady, turbulent, isothermal, and incompressible. The Navier–Stokes equations are resolved with the `simpleFoam` OpenFOAM® solver (Weller et al., 1998), and are given by

$$\nabla \cdot (\rho \mathbf{u}) = 0, \tag{1}$$

$$\nabla \cdot (\rho \mathbf{u}\mathbf{u}) = -\nabla p + \nabla \cdot \left[(\mu + \mu_T)(\nabla \mathbf{u} + \nabla \mathbf{u}^T)\right] + \mathbf{f_B}, \tag{2}$$

where ρ represents the fluid density, $\mathbf{u}$ is the velocity vector, p is the pressure field, μ is the fluid viscosity, and $\mathbf{f_B}$ represents the linear momentum source term vector. μ_T represents the contribution of turbulent viscosity and is calculated by equation (3), that is:

$$\mu_T = \rho\,\tilde{\nu}\,\frac{\chi^3}{\chi^3 + C_{\nu 1}^3}, \tag{3}$$

where $\chi = \dfrac{\tilde{\nu}}{\nu}$. Using the Spalart–Allmaras turbulence model (Spalart & Allmaras, 1992), the turbulent viscosity is calculated as a function of the modified kinematic viscosity ($\tilde{\nu}$) field, given by equation (4):

$$\frac{\partial \tilde{\nu}}{\partial t} = C_{b1}(1 - f_{t2})\tilde{S}\tilde{\nu} + \frac{1}{\sigma}\left[\nabla \cdot ((\nu + \tilde{\nu})\nabla\tilde{\nu}) + C_{b2}(\nabla\tilde{\nu})^2\right] - \left[C_{w1}f_w - \frac{C_{b1}}{\kappa^2}f_{t2}\right]\left(\frac{\tilde{\nu}}{d}\right)^2, \tag{4}$$

where C_{b1}, C_{b2}, C_{w1}, $C_{\nu 1}$, f_w and σ are experimentally defined turbulence model coefficients, according to Spalart and Allmaras (1992).

The Spalart-Allmaras model was designed specifically for aerospace applications and aerodynamic flows involving wall-bounded flows, and has been shown to provide good results for boundary layers subjected to adverse pressure gradients. It is known for being a one, equation model, which is easier to solve numerically, as the solution is likely to be close to linear.

Mesh and numerical model

To create the mesh, the computational tool *snappyHexMesh*® was used (Weller et al., 1998). It is a framework designed to create high-quality, unstructured, and body-fitted computational grids. It operates on top of an initial background hexahedral mesh and refines it locally around geometrical surfaces and flow regions of interest.

A structured background mesh is processed by the tool that approximates it to a geometry provided through refinement iterations, as well as having other mesh controls such as refinement levels and the addition of layers of elements. Figure 2 presents the background mesh used for the simulations and details of the mesh refinement over the airfoil with a generic flap.

Figure 2 - Background mesh with details and refined regions over the airfoil: (a) near wake, (b) mesh over the airfoil with flap, and (c) trailing edge.

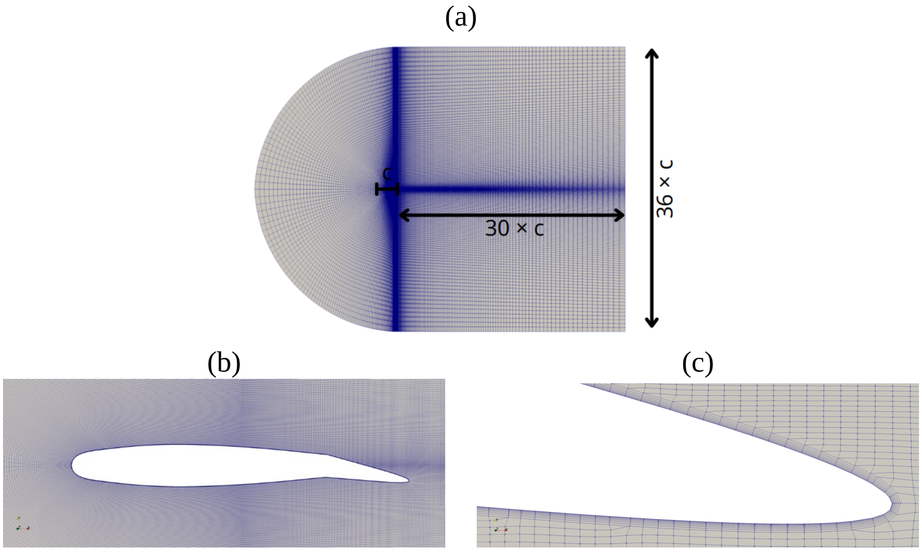

Note that the central region, corresponding to the near-wake area, Figure 2(a), is refined by two levels, and a prism layer mesh is created near the surface to properly capture the behavior of the flow's boundary layer, Figure 2(b). Finally, Figure 2(c) shows the refined mesh at the trailing-edge region of the airfoil.

The chord of the airfoils used is unitary, and the dimensions of the computational domain generated are proportional to this length.

Boundary conditions

The boundary conditions used in this work are the following: the inlet and outlet are set as *freestream*, which is a generic boundary condition that provides a free-stream condition whereby the mode of operation switches between fixed value and zero gradient based on the sign of the flow. If the flow enters the surface, it is allocated as fixed value, and if it exits, the *zeroGradient* condition is applied for all variables.

The value U_α corresponds to the initial velocity vector, which depends on the chosen angle of attack (α) but always has an absolute value of 25 m/s. For the turbulent viscosity, the fixed value of the input is approximated to the fluid viscosity, while for the Spalart-Allmaras model modified viscosity, Langley Research Center (2024) recommends a value between three and five times the fluid's viscosity.

Results and discussion

Mesh convergence

The meshes used for the simulations in this work were generated using the methodology described, meeting minimum quality requirements that eliminate highly skewed, non-orthogonal, or negative-volume cells. The variable y^+ is an important dimensionless number that represents the size of the first element near the wall.

Figure 3 shows the distribution of this number over the surfaces of two airfoils; for the sake of brevity, they can be considered representative of all simulations. A y^+ value close to 1 allows the resolution of the viscous sublayer, and its value remains below 5 for most of the surface, although it exceeds this value for small portions of the leading edge. In this way, it was not necessary to use wall laws .

Figure 3 - y+ distribution along the airfoil surfaces: (a) airfoil no flap, (b) flap deflection.

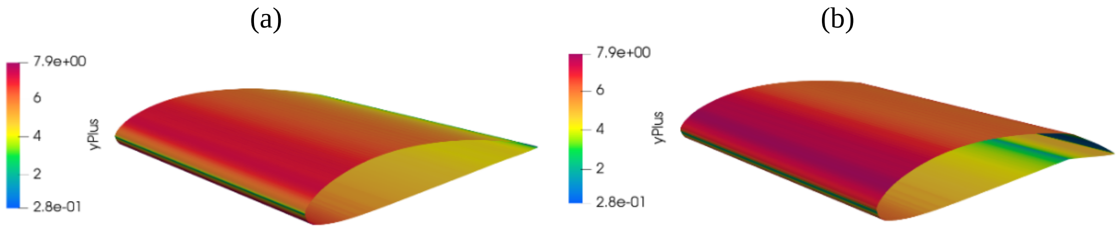
(a)

(b)

Additionally, mesh independence tests were carried out for those flap configurations to ensure that the results analyzed were not a function of mesh refinement. To do this, Figure 4 shows the lift (C_l), and drag (C_d) coefficient results for the simulations of the flow over the clean airfoil, with a plain flap for different angles of attack.

Figure 4 - Influence of mesh refinement on lift and drag coefficients: (a)–(b) clean airfoil and (c)–(d) plain flap.

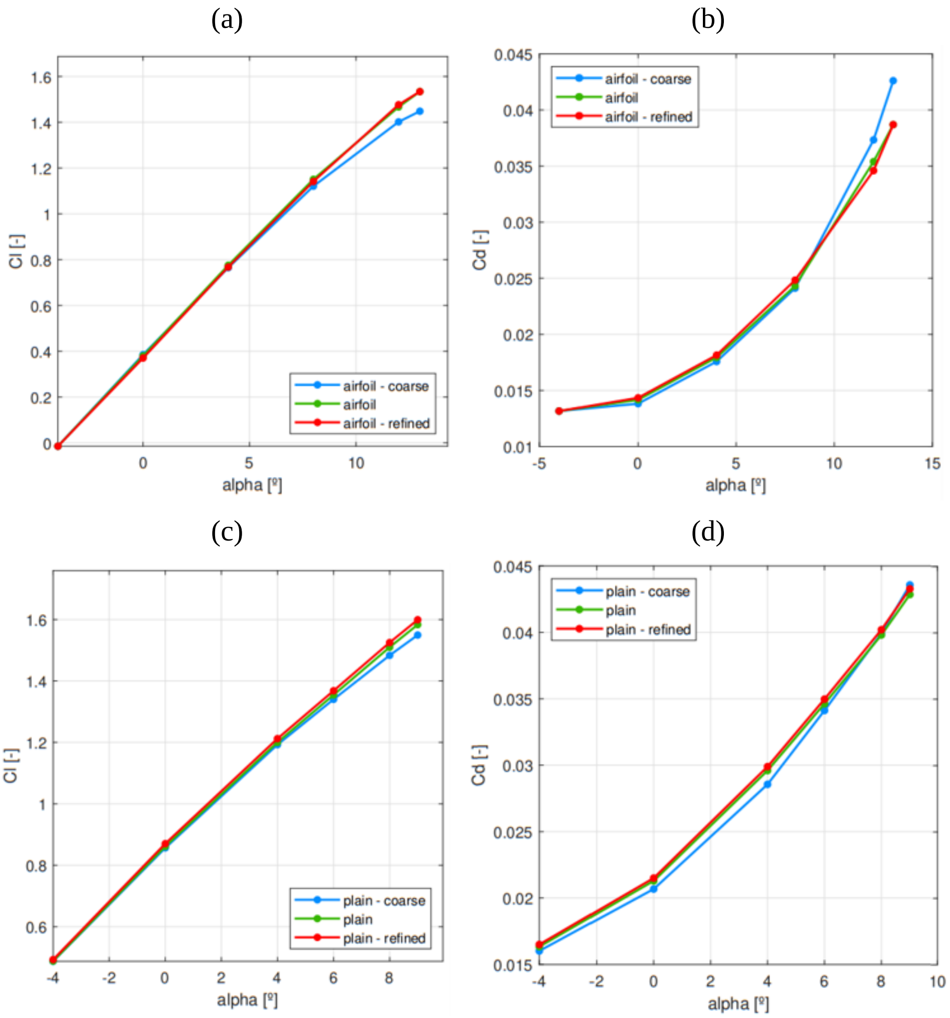
(a)

(b)

(c)

(d)

Table 1 presents the mesh properties such as the number of cells and layers of elements near the airfoil are shown for comparison.

Table 1 - Properties of meshes used in this work.

Mesh	**Clean airfoil**		**Plain flap**	
	Nº of cells	**Nº of layers**	**Nº of cells**	**Nº of layers**
Coarse	440640	4	424451	4
Medium	464113	5	780796	5
Refined	1746817	9	823752	9

Literature Comparison – Validation

To verify the accuracy of the results obtained in the previous sections, additional comparisons were performed using data available in the literature from Jawahar et al. (2018), Kumar and Kumar (2013), and Ladson (1988). Replicating the geometries and boundary conditions reported by these authors, numerical simulations of different airfoils were carried out using the OpenFOAM® software.

Ladson (1988)

The study performed by Ladson (1988) carried out a range of wind tunnel experiments using the NACA 0012 airfoil, varying the Reynolds number, Mach, and angle of attack, and analyzing the results of the aerodynamic coefficients. An angle of attack range between -4° and 15° was simulated for a Reynolds number of $Re = 6 \times 10^6$.

The velocity entering the domain was set at 51.4815 m/s, and the turbulence model used was Spalart–Allmaras. Figure 5 contains a comparison of the lift and drag coefficient results obtained.

Figure 5 - Aerodynamic coefficients obtained in this work and by Ladson (1988): (a) lift, and (b) drag.

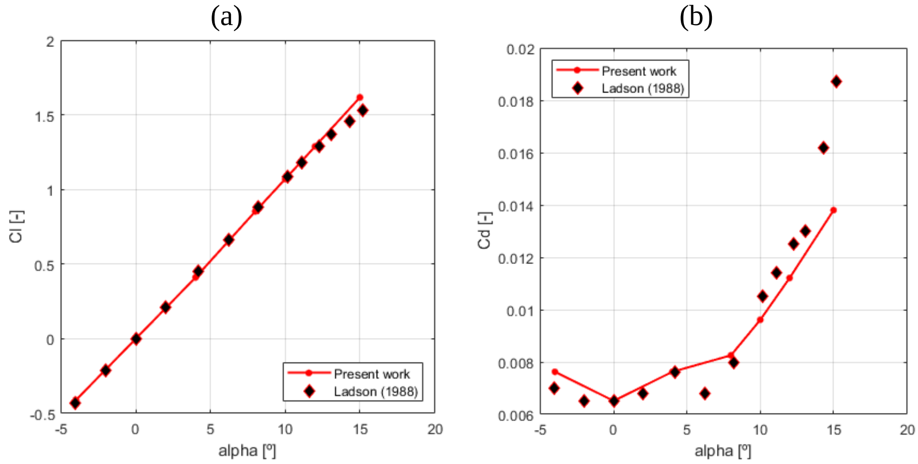

It is possible to see a match in the lift coefficient (C_l) and drag coefficient (C_d) data; Figures 5(a) and 5(b), respectively, even though the difference between the drag results is greater.

According to Avraham (2024), the drag force is inherently more difficult to predict compared to other phenomena, because it depends on several factors that are calculated in a numerical simulation; imperfections in the turbulence model, mesh limitations, and sensitivity to convergence affect this result more considerably.

Jawahar et al. (2018)

Jawahar et al. (2018) experimentally analyzed the performance of a NACA 0012 airfoil with flaps. Results of lift, drag, and wake flow coefficients were obtained with different flap camber profiles over a wide range of angles of attack and Reynolds numbers. The authors carried out experiments in a wind tunnel with flap airfoils deflected at 5° and 10° with an air inlet velocity equal to 25 m/s, corresponding to a Reynolds number $Re = 3.5 \times 10^5$.

To replicate the results of the experiments for the Hinged Flap, these same properties were adjusted in the OpenFOAM® software routine. The results obtained in the simulation and those obtained by the author are shown in Figure 6.

Figure 6 - Aerodynamic coefficients obtained in this work and by Jawahar et al. (2018): (a) lift, and (b) drag.

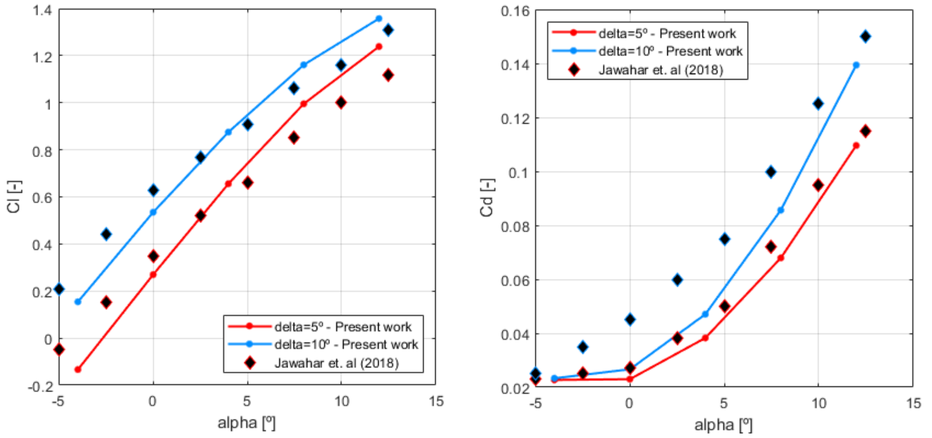
(a) (b)

The behavior of the coefficients, Figure 6(a) and 6(b), is like that discussed previously in the work by Ladson (Ladson, 1988), with the lift coefficient results showing greater accuracy than the drag results.

Figure 7 shows a wake flow field comparison of both works: obtained by numerical simulation in OpenFOAM® using the velocity fields, and experimentally using hot wire anemometry in the wind tunnel. Dimensionless velocity profiles are shown as a function of vertical position for different horizontal chord distances, for the airfoil with flap deflection, $\delta = 5°$, and null angle of attack, $\alpha = 0°$.

Figure 7 - Wake velocity profiles obtained for $\delta = 5°$ and $\alpha = 0°$: (a) $x/c = 1.01$, (b) $x/c = 1.15$, (c) $x/c = 1.215$ and (d) $x/c = 1.515$.

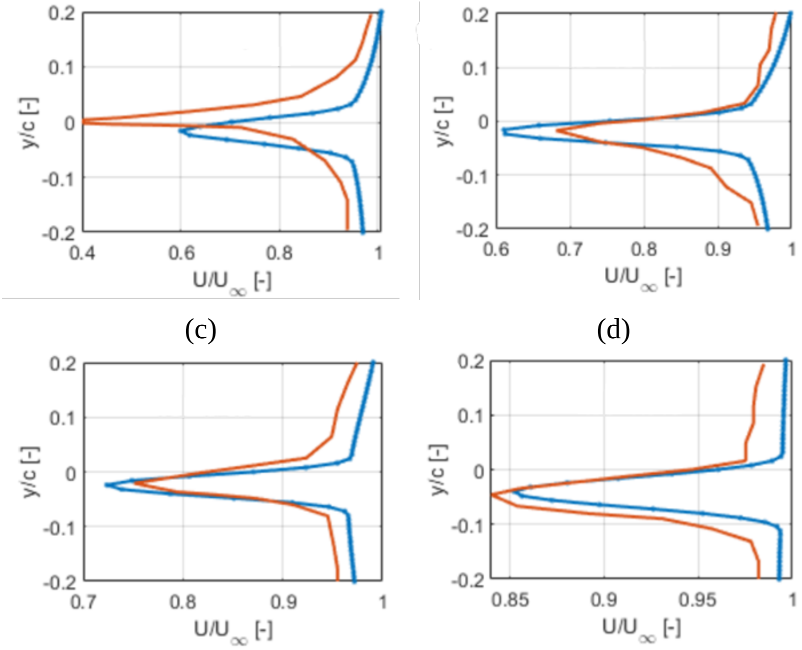
(a) (b) (c) (d)

It is possible to observe the same behavior of translation of the peak velocity and decrease of the amplitude when increasing the distance from the chord; Figures 7(a)–7(d), mainly the farther away from the surface the velocity field is analyzed.

Kumar and Kumar (2013)

Kumar and Kumar (2013) performed numerical simulations of the aerodynamic flow over a NACA0012 airfoil with a plain flap at different angles of attack and flap deflection. Results for the coefficients of lift (C_l) and drag (C_d) are compared for four values of flap deflection ($\delta = 0°, 5°, 10°$, and $15°$) and angle of attack ($\alpha = 0°, 4°, 8°$, and $12°$). The authors used the $k-\varepsilon$ turbulence model and a velocity entering the computational domain equal to 25 m/s, which results in a Reynolds number $Re = 1.7 \times 10^6$.

In Figure 8, the lines represent the results obtained by OpenFOAM®, while the diamonds show the author's results.

Figure 8 - Aerodynamic coefficients obtained in this work and by Kumar and Kumar (2013): lift, and (b) drag.

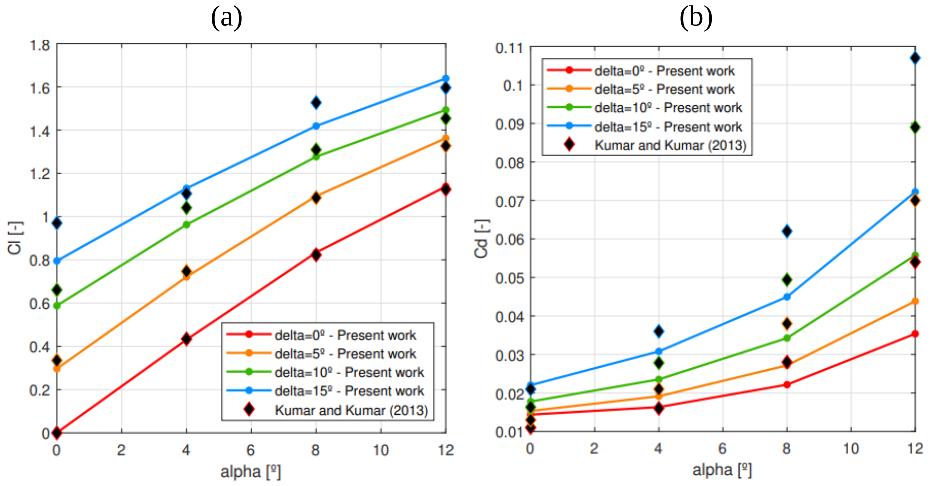

The results, Figures 8(a) and 8(b), were like the reference data in terms of lift coefficient, while in terms of drag, the simulation proved to be more accurate for moderate angles of attack.

High-lift configuration comparisons

A compilation of the results of the lift and drag coefficients for the NACA4412 airfoil equipped with different flap configurations is shown in Figure 9, where each type of flap is identified by a color.

Figure 9 - Aerodynamic coefficients for the clean airfoil and different flap configurations as a function of the angle of attack: (a) lift, and (b) drag.

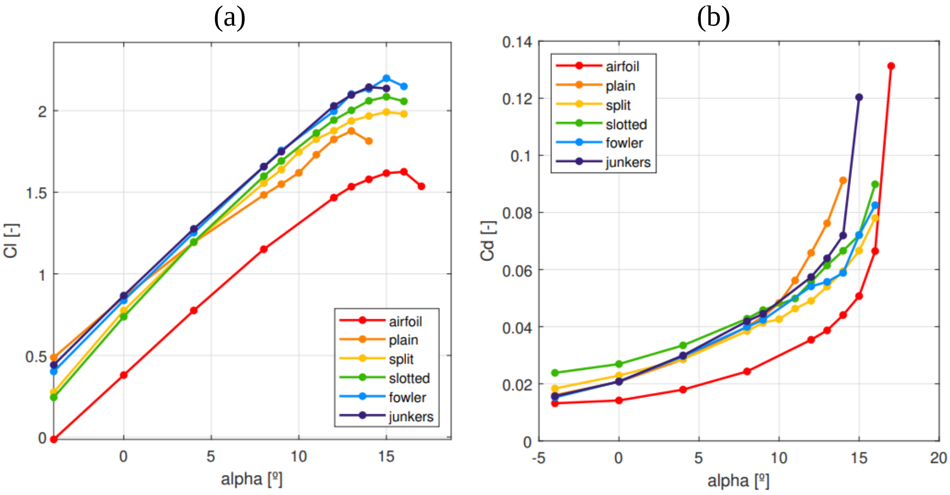

Clean Airfoil

The results are compared with the control group: the clean NACA4412 airfoil, designated as "airfoil". Figure 10 shows the velocity fields and pressure coefficient distribution of the flow around the airfoil for different angles of attack; $\alpha = 0°$ and $\alpha = 16°$, respectively.

Figure 10 - Velocity and pressure coefficient distributions over the clean airfoil: (a)–(b) velocity fields at $\alpha = 0°$ and $\alpha = 16°$; (c)–(d) pressure coefficient distributions at $\alpha = 0°$ and $\alpha = 16°$.

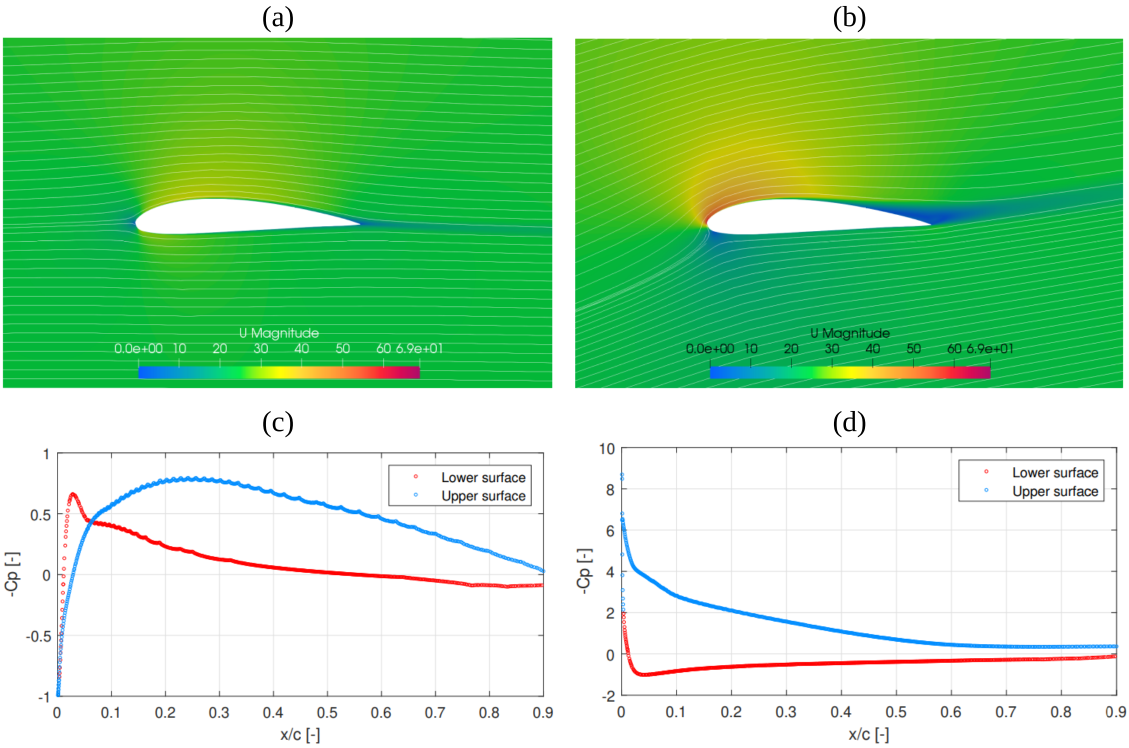

The velocity gradient observed on the upper surface increases with the angle; Figures 10(a) and 10(b). It is possible to verify the behavior of the coefficients for the clean airfoil in previous Figure 9, where the lift has a linear region and a maximum coefficient $C_{l\,\max} = 1.626$, which occurs at angle $\alpha = 16°$. For drag, it has its minimum value for α between $-4°$ and $0°$, increasing along with the angle of attack. When $\alpha = 0°$, the flow remains adhered to almost the entire surface, but begins to detach; up until when $\alpha = 16°$, it detaches near the leading edge, explaining the drop in lift generated.

The distribution of the pressure coefficient,Figures 10(c) and 10(d), for identical angles of attack (AOAs), reveals distinct regions of high pressure that coincide with the locations of the stagnation points. As the boundary layer begins to detach, the low pressure region over the upper surface progressively diminishes, while the associated pressure gradient becomes increasingly steep, indicating the onset of flow separation. The pressure differential between the upper and lower surfaces constitutes the main mechanism through which lift is generated, as it results from the flow deflection around the wing, a behavior consistently observed throughout this study. At lower angles of attack, this pressure difference remains relatively small, producing limited lift; however, as the angle of attack increases, the pressure gradient intensifies markedly, leading to a significant rise in lift generation.

Plain flap

The lift and drag coefficients for the plain flap are identified by the color orange and the label "plain" in previous Figure 9. The lift generated is greater as the flap deflects, while the stall angle observed is smaller, close to $13°$, reaching a maximum lift coefficient $C_{l\,\max} = 1.884$. The increase in the maximum lift coefficient compared to the clean airfoil was $\Delta C_{l\,\max} = 0.258$, a result close to that found experimentally by Cahill (1949), of $\Delta C_{l\,\max} = 0.235$. The author analyzed airfoils from the NACA family for a range of Reynolds numbers $Re = 6 \times 10^5$ and with flap chords equal to 20% and 30% of the airfoil length. Meanwhile, the increase in the drag coefficient generated with flap deflection is to be expected and is more evident for steeper attack angles. Figure 11 presents the velocity field for several simulations performed on the plain flapped airfoil.

Figure 11 - Velocity and pressure coefficient distributions over the clean airfoil: (a)–(b) velocity fields at $\alpha = 0°$ and $\alpha = 13°$; (c)–(d) pressure coefficient distributions at $\alpha = 0°$ and $\alpha = 13°$.

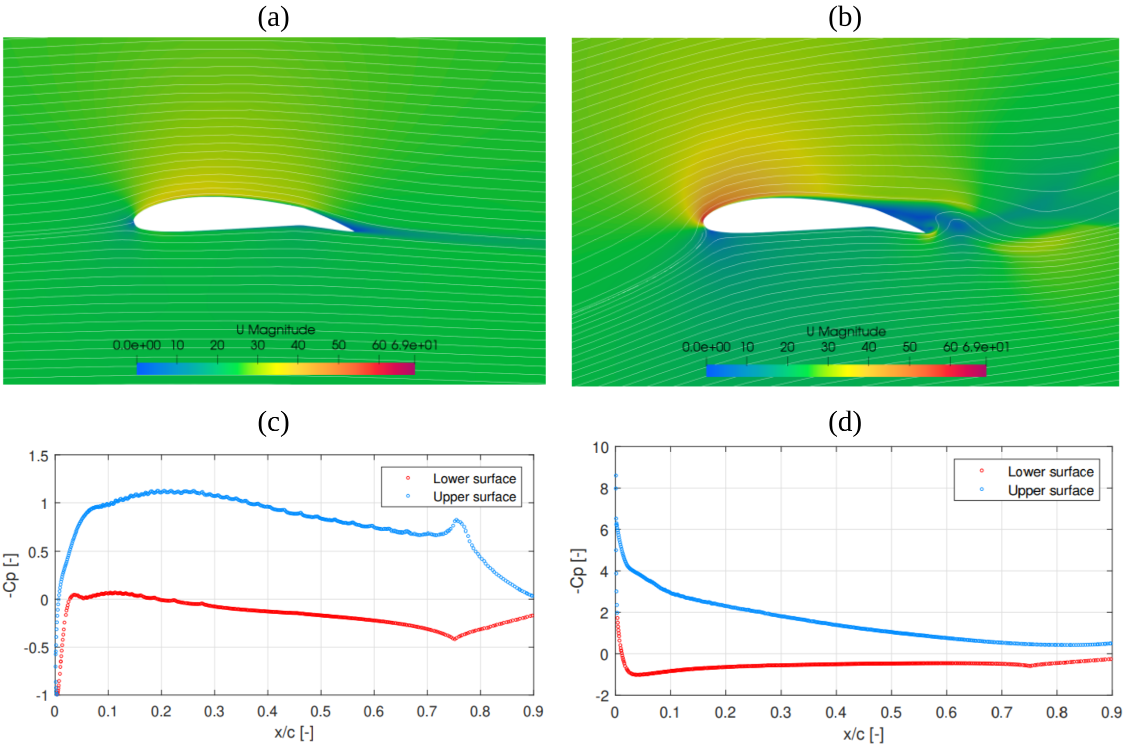
(a) (b) (c) (d)

It is possible to observe the same behaviors identified in the airfoil without deflection, namely the stagnation points and the region of high velocity caused by the flow deflection as it follows the surface geometry, a phenomenon known as *upwash*. Additionally, as the angle of attack increases, the detachment of the boundary layer moves closer to the leading edge, occurring at much smaller angles compared to the clean airfoil, which significantly influences the aerodynamic performance and stall characteristics.

The behavior of the pressure distribution showed a more pronounced pressure gradients compared to the previous case. This explains the increased generation of both lift and drag across all angles of attack. For smaller inclinations, a noticeable pressure peak can be observed near 75% of the airfoil chord on both surfaces. This peak results from the abrupt change in surface inclination caused by the flap deflection, which induces a localized bending in the flow, increasing velocity in that region. However, as α increases, this phenomenon becomes less prominent, as the boundary-layer detachment extends beyond the flap's hinge point, altering the pressure distribution and flow characteristics.

Split flap

As for the split flap, in previous Figure 9 it is represented by the color yellow. In terms of the lift generated, its performance is better than the previous geometry. Despite generating less lift for low and negative angles, the split flap has a steeper lift curve, which results in higher lift levels for larger angles of attack. In addition, the stall angle was greater than when using the plain flap, the lift curve reaching its maximum $C_{l_{\max}} = 1.981$, which occurs at angle $\alpha = 15°$. The split flap generates greater drag at low angles of attack, but it proved to be more efficient than the plain flap for moderate angles of attack.

Compared to the clean airfoil, the split flap generates an increase in maximum lift of $\Delta C_{l_{\max}} = 0.367$, a result close to that extrapolated from the work by Gudmundsson (2013), who reports $\Delta C_{l_{\max}} = 0.383$ for split flaps coupled to NACA-family airfoils analyzed in a lower Reynolds range, $\mathrm{Re} = 6 \times 10^5$, with chord ratios equal to 0.2 and 0.3. In the velocity field of Figures 12(a) and 12(b), it is possible to observe the behavior of the flow at the trailing edge of the airfoil.

Figure 12 - Velocity and pressure coefficient distributions over the clean airfoil: (a)–(b) velocity fields at $\alpha = 0°$ and $\alpha = 15°$; (c)–(d) pressure coefficient distributions at $\alpha = 0°$ and $\alpha = 15°$.

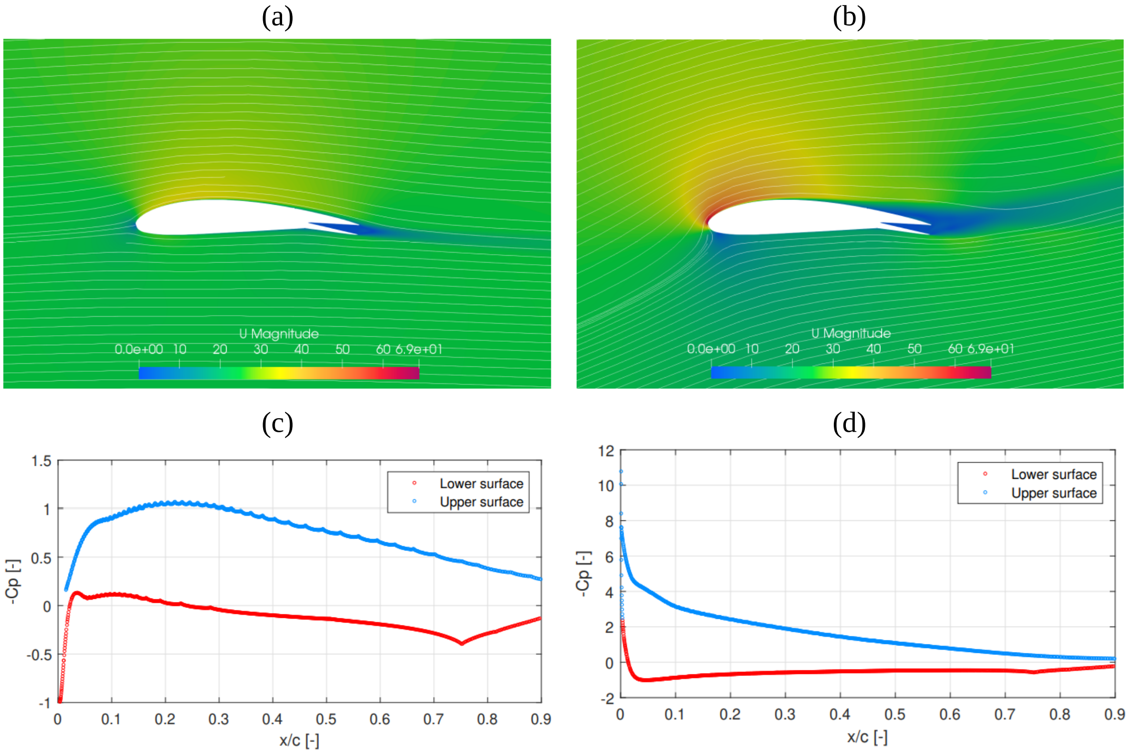

The split flap, unlike the other flaps analyzed in this paper, was not studied at its optimum deflection between $60°$ and $70°$. However, to preserve the original intention of comparing different airfoil configurations in similar physical conditions, the deflection angle was chosen to be $10°$, since simulations of other configurations would not be representative of normal flight conditions for larger angles. Because the deflection of this type of flap occurs only on the lower surface of the airfoil, the flow is not significantly deflected at low angles of attack, generating little downwash and less lift than the plain flap, for example.

However, a positive aspect to note is that as the upper surface does not change direction abruptly, the boundary-layer detachment occurs at greater angles, making it possible to delay the stall. In addition, it is possible to see a large separation between the flap blades at the trailing edge and the wake behind the airfoil. The pressure coefficient distribution has a similar pattern as seen in previous cases.

The presence of an unchanged top surface with a smooth transition prevents the formation of low-pressure peaks near the flap's hinge line. For larger angles of attack, the negative pressure gradient on the upper surface in the first 25% of the chord results in greater lift.

Slotted flap

The aerodynamic coefficients of the flow over the slotted flap are identified with the label *slotted* and the color green in previous Figure 9. When the lift curve is analyzed, the behavior is very similar for both the plain flap and the split flap with the same deflection angle. However, as expected, the stall angle is greater than the first case described, this time peaking at $\alpha = 15°$ and reaching a higher level of lift than both devices shown, with $C_{l_{\max}} = 2.085$.

The effect of the slot is comparable to that of the deflection of the lower surface of the flap. As for drag, this type of flap showed high levels at low angles of attack but was close to the other configurations, reaching a maximum aerodynamic efficiency of $L/D = 37.43$ when $\alpha = 8°$. Figure 13(a) and 13(b) shows the velocity fields together with the flow current lines for the slotted flap.

The velocity behavior near the leading edge resembles previous cases; however, the slot significantly alters the flow dynamics. The trailing edge effectively acts as a secondary airfoil, inducing a stagnation point on the lower surface and a high-velocity region as the fluid accelerates and follows the surface curvature.

Figure 13 - Velocity and pressure coefficient distributions over the clean airfoil: (a)–(b) velocity fields at $\alpha = 0°$ and $\alpha = 15°$; (c)–(d) pressure coefficient distributions at $\alpha = 0°$ and $\alpha = 15°$.

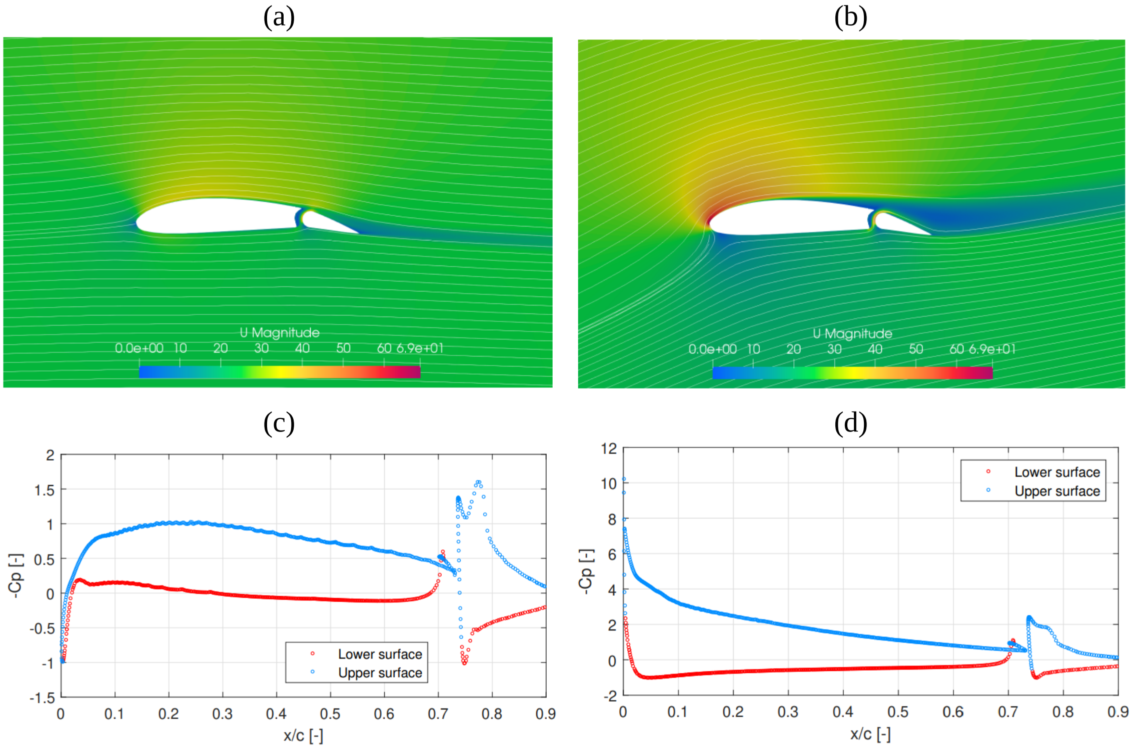

(a) (b) (c) (d)

The slot draws flow from the lower surface and injects it into the upper side, maintaining flow attachment even at high angles of attack by re-energizing the boundary layer and delaying separation. Combined with the lift coefficient results, this explains the lower lift at small angles of attack, where downwash is weaker than in a plain flap configuration.

The pressure coefficient distribution shows a reduced pressure difference between the upper and lower surfaces due to the fluid exchange through the slot. At low angles of attack, higher pressure occurs near the trailing edge (around 75% chord) on both surfaces, while increasing the angle of attack shifts lift generation toward the leading edge (first 25% of the chord) with relatively constant pressure on the flap.

Fowler flap

The lift coefficient curve of the fowler flap is shown in previous Figure 9, represented by the color blue. Among the flap configurations analyzed, this is the one with the greatest potential for generating lift. This is due to the property of Fowler flaps of significantly increasing the chord of the airfoil in addition to rotation, keeping the flow attached to the surface while it is deflected.

As the planform area of the airfoil essentially increases with the deflection of the flap, the reference area used to calculate the coefficients is not unitary but must be 1.25. A stall angle of $\alpha = 15°$ is observed, but this generates the highest maximum lift coefficient, $C_{l_{\max}} = 2.199$, the inclination is greater than in the previous cases due to the movement of rotation and translation of the flap. This results in high aerodynamic efficiency, reaching a maximum of $L/D = 42.29$ when $\alpha = 4°$. The streamlines in Figure 14(a) and 14(b) show the velocity fields for the Fowler flap.

It is possible to observe the stagnation point and the bending region of the flow just as it occurred in the flow over the slot flap. Essentially, the flap acts as an extension of the airfoil, keeping the flow adhered to the surface and deflecting it further, generating more lift. The main difference is seen in the pressure distribution on the surface. Firstly, the pressure gradient extends over the entire surface, further separating the flow into a high-pressure and low-pressure region. Positioned beyond the unit length of the airfoil, the flap essentially increases the contact area of the pressure resulting from the flow, generating an even greater force.

Figure 14 - Velocity and pressure coefficient distributions over the clean airfoil: (a)–(b) velocity fields at $\alpha = 0°$ and $\alpha = 15°$; (c)–(d) pressure coefficient distributions at $\alpha = 0°$ and $\alpha = 15°$.

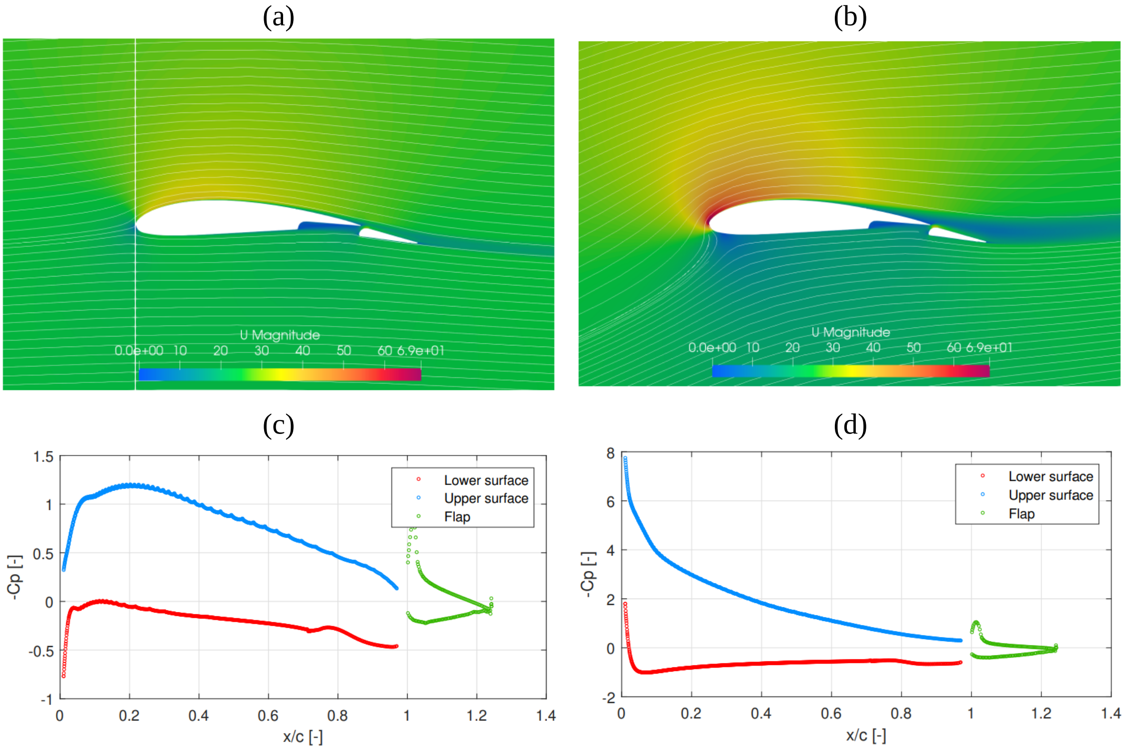

Junkers flap

To analyze the Junkers flap, it is necessary to evaluate both its rested and deployed positions, since the presence of the flap at rest in the lower section influences the flow around the airfoil. In Figure 15 the lift and drag coefficients are shown as a function of the angle of attack for the two positions of this type of flap, together with those of the clean airfoil, for comparison. It's worth noting that, like the Fowler flap, the effective area of the Junkers flap also equals 1.25.

Figure 15 - Coefficients for the clean airfoil and Junkers flap configurations as functions of the angle of attack: (a) lift and (b) drag.

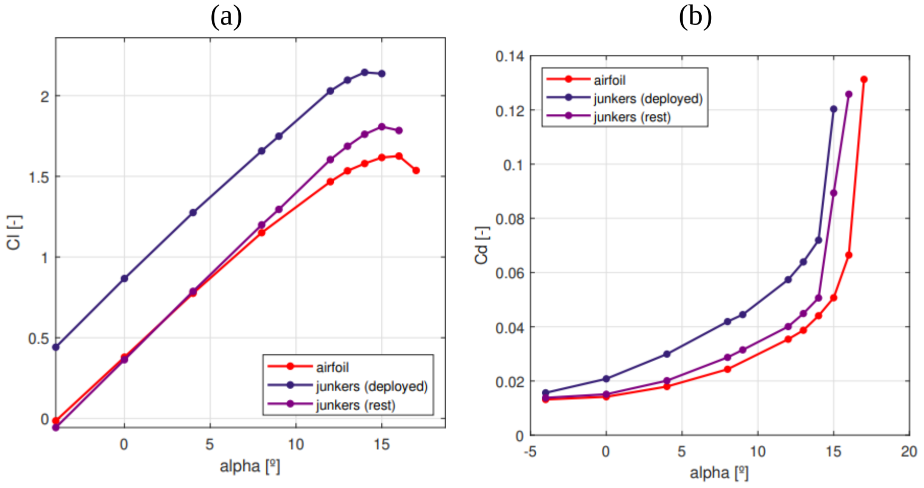

When the flap is in its initial position, there is a higher maximum lift coefficient than the clean airfoil: $C_{l_{\max}} = 1.808$, which is achieved at a lower angle of attack, $\alpha = 15°$. The behavior of the extended flap is similar, but the deflection of the flap results in higher initial lift values even for low angles of attack, resulting in a $C_{l_{\max}} = 2.144$ when $\alpha = 14°$. As for drag, the increase for the rest position compared to the clean airfoil is negligible.

Figure 16 shows the velocity fields and streamlines around the airfoil with the Junkers flap for both positions: (a)–(b) rested and (c)–(d) deflected. For the resting position, the flow is like the clean airfoil's when the AOA is low enough. As the incidence increases, the flap, even with zero deflection, contributes by bending the flow, which accommodates itself to deviate from the surface. As the angle of attack increases, it is possible to observe a common phenomenon for this type of compound airfoil: the detachment of the boundary layer does not only occur on the main element, but on the flap as well.

Figure 16 - Velocity and pressure coefficient distributions over the clean airfoil: (a)–(b) velocity fields at $\alpha = 0°$ and $\alpha = 15°$; (c)–(d) pressure coefficient distributions at $\alpha = 0°$ and $\alpha = 15°$.

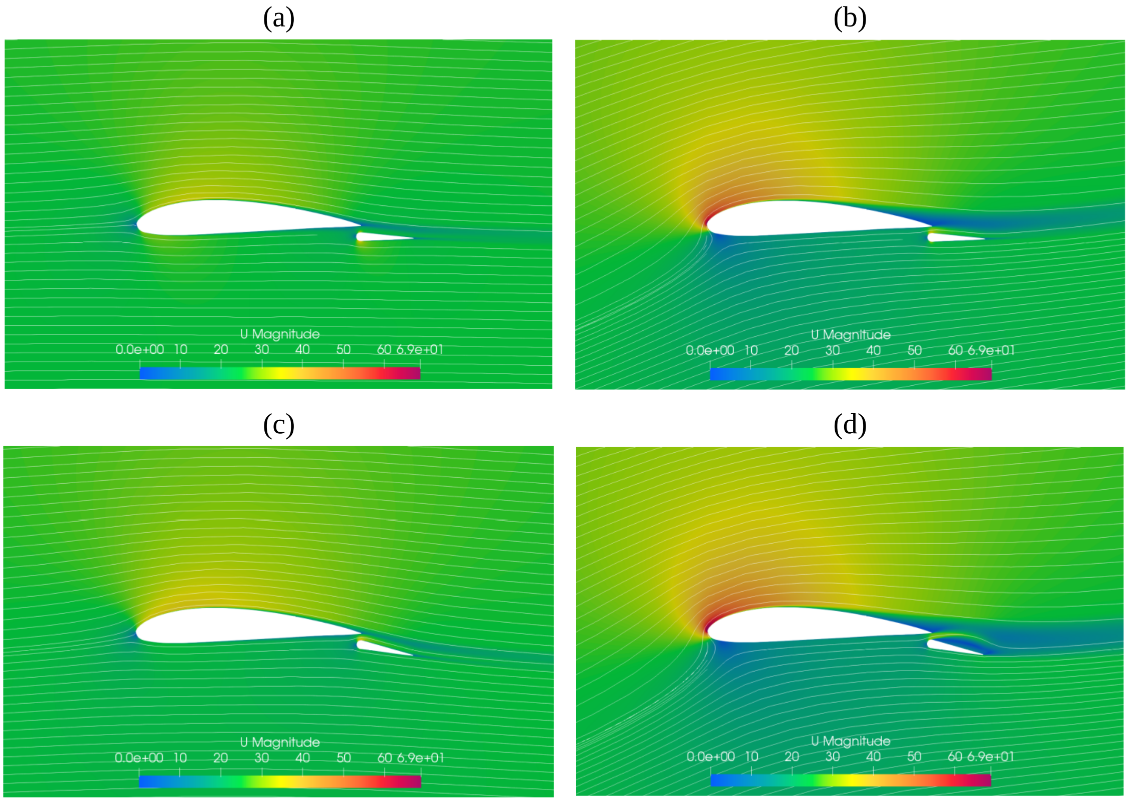
(a) (b) (c) (d)

Like the Fowler flap, the flap further divides the lower high-pressure region and the upper low-pressure region when the angle of attack is greater in both flap positions, as can be noted in the Figure 17. Analyzing the deployed flap configuration, it is possible to see a pressure difference between the lower and upper surfaces of the flap. In addition, both the negative and positive pressure gradients become more intense than in the case of flaps with only rotational movement (plain, split and slotted). The negative pressure to which the top surface of the flap is subjected decreases dramatically for greater angles, due to the separation of the boundary layer that also occurs in the flap, as noted earlier.

Figure 17 - Pressure coefficient distribution along the airfoil with Junkers flap for (a) $\alpha = 0°$ and (b) $\alpha = 15°$.

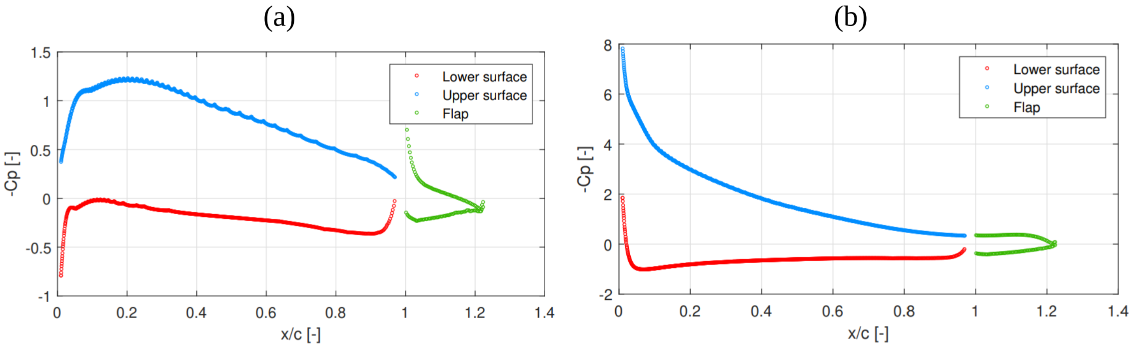
(a) (b)

Conclusions

The main objective of this work was to develop and validate a robust numerical approach for simulating flows around airfoils with high-lift devices, by using the CFD opensource code OpenFOAM®. Beyond successfully reproducing experimental and numerical benchmarks for lift and drag, this study also contributes by consolidating a systematic workflow, covering mesh validation, solver setup, and post-processing, that can be directly reused for future aerodynamic investigations. This structured approach represents a step forward in the open-source CFD community, offering a validated alternative to commercial tools for high-lift device analysis.

The results confirmed the reliability of the methodology, with mesh convergence and validation against the literature ensuring consistency. Among the configurations studied, the Fowler flap demonstrated the greatest lift enhancement with only a modest drag penalty, confirming its suitability for applications where takeoff and landing performance is critical. The slotted flap also showed strong potential, particularly for designs requiring a balance between lift augmentation and structural simplicity. Junkers flaps, although capable of similar lift levels, highlight a trade-off between performance gains and structural penalties, which limits their widespread adoption. Conversely, the split and plain flaps reinforced their limited aerodynamic usefulness under modern design criteria.

The novelty of this work lies in bridging validated CFD procedures with a comparative study of classical flap configurations under consistent conditions, something often fragmented in the literature. The findings not only reaffirm why Fowler and slotted flaps dominate current practice, but also provide a reliable computational framework for exploring unconventional high-lift concepts or optimizing existing ones. Potential applications include preliminary aircraft design studies, educational use in aerodynamics courses, and as a foundation for integrating CFD-based optimization or AI-driven design exploration.

Acknowledgments

The authors would like to thank the Financiadora de Estudos e Projetos (FINEP - 0138/11) for funding the CPAERO (Experimental Aerodynamics Research Center) from Federal University of Uberlandia (UFU).

Author Contributions

T. R. Castro: data curation, formal analysis, investigation, methodology, validation, writing – review and editing. **O. Almeida**: conceptualization, investigation, methodology, supervision, writing – review and editing.

Conflicts of Interest

The authors declare no conflict of interest.

References

Avraham, T. (2024). What a drag. https://cfdisraelblog.com/2024/01/19/what-a-drag-part-iii/

Bhandari, S. N. (2019). CFD analysis of flap of airplane wing span at subsonic speed. *International Journal of Industrial Engineering and Technology*, *11*(1), 1–7. http://www.irphouse.com/ijiet19/ijietv11n1_01.pdf

Cahill, J. F. (1949). *Summary of section data on trailing-edge high-lift devices (NACA-TR-938)*. National Advisory Committee for Aeronautics. https://ntrs.nasa.gov/citations/19930092003

Dal Monte, A., Castelli, M. R., & Benini, E. (2012). A retrospective of high-lift device technology. *Proceedings of World Academy of Science, Engineering and Technology*, (71), 1979.

Fonseca, W. D. P., Reis, M. W. F., Dias, P. F. L., & Sousa, L. M., Filho. (2019). CFD Analysis of airfoils with flaps for low Reynolds numbers. *Revista de Engenharia e Pesquisa Aplicada*, *4*(4), 93–101. https://doi.org/10.25286/repa.v4i4.1240

Gudmundsson, S. (2013). *General Aviation Aircraft Design: Applied Methods and Procedures*. Butterworth-Heinemann.

Jawahar, H. K., Ai, Q., & Azarpeyvand, M. (2018). Experimental and numerical investigation of aerodynamic performance for airfoils with morphed trailing edges. *Renewable Energy*, *127*, 355–367. https://doi.org/10.1016/j.renene.2018.04.066

Kumar, M. S., & Kumar, K. N. (2013). Design and computational studies on plain flaps. *Bonfring International Journal of Industrial Engineering and Management Science*, *3*(2), 33–39. https://doi.org/10.9756/bijiems.4259

Ladson, C. L. (1988). *Effects of independent variation of Mach and Reynolds numbers on the low-speed aerodynamic characteristics of the NACA 0012 airfoil section*. NASA. https://ntrs.nasa.gov/api/citations/19880019495/downloads/19880019495.pdf

Langley Research Center. (2024). The Spalart-Allmaras turbulence model. https://turbmodels.larc.nasa.gov/spalart.html

Meredith, P. T. (1993). Viscous phenomena affecting high-lift systems and suggestions for future CFD development. *AGARD Conference Proceedings*, *515*, 19.1–19.8. https://jglobal.jst.go.jp/en/detail?JGLOBAL_ID=200902174678111864

Murayama, M., Lei, Z., Mukai, J., & Yamamoto, K. (2006). CFD Validation for High-Lift Devices: Three-Element Airfoil. *Transactions of The Japan Society for Aeronautical and Space Sciences*, *49*(163), 40–48. https://doi.org/10.2322/tjsass.49.40

Murayama, M., & Yamamoto, K. (2004). Numerical Simulation of High Lift Configurations Using Unstructured Mesh Method. In *International Congress of the Aeronautical Science* [Proceedings]. 24th International Congress of the Aeronautical Science, Yokohama, Japan. https://icas.org/icas_archive/ICAS2004/PAPERS/414.PDF

Sarjito, Aklis, N., & Hartanto, T. (2017). An optimization of flap and slat angle airfoil NACA 2410 using CFD. *AIP Conference Proceedings*, *1831*(1), 020038. https://doi.org/10.1063/1.4981179

Silva Oliveira, A. (2017). *Low Reynolds Number Fowler Flap Design* [Dissertação Mestrado, Universidade da Beira Interior]. https://ubibliorum.ubi.pt/bitstream/10400.6/7916/1/5366_10606.pdf

Spalart, P., & Allmaras, S. (1992). A one-equation turbulence model for aerodynamic flows. In American Institute of Aeronautics and Astronautics, *AIAA Meeting Paper* [Proceedings]. 30th Aerospace Sciences Meeting and Exhibit, Reno, USA. https://doi.org/10.2514/6.1992-439

Tan, H. (2020). *CFD Analysis of a Wind Turbine Airfoil with Flap* [Master of Science, McKelvey School of Engineering]. https://doi.org/10.7936/gdhb-zg49

van Dam, C. P. (2002). The aerodynamic design of multi-element high-lift systems for transport airplanes. *Progress in Aerospace Sciences*, *38*(2), 101–144. https://doi.org/10.1016/s0376-0421(02)00002-7

Weller, H. G., Tabor, G., Jasak, H., & Fureby, C. (1998). A tensorial approach to computational continuum mechanics using object-oriented techniques. *Computers in Physics*, *12*(6), 620–631.